Supplemental Document

Biomedical Optics EXPRESS

# Single-objective high-resolution confocal light sheet fluorescence microscopy for standard biological sample geometries: supplement

STOYAN YORDANOV,[1,4] KONSTANTIN NEUHAUS,[1,2,4] RAIMO HARTMANN,[1] FRANCISCO DÍAZ-PASCUAL,[1] LUCIA VIDAKOVIC,[1] PRAVEEN K. SINGH,[1] AND KNUT DRESCHER[1,2,3,*]

[1] *Max Planck Institute for Terrestrial Microbiology, Karl-von-Frisch-Straße 10, 35043 Marburg, Germany*
[2] *Department of Physics, Philipps-Universität Marburg, Renthof 5, 35037 Marburg, Germany*
[3] *Biozentrum, University of Basel, Spitalstrasse 41, CH-4056 Basel, Switzerland*
[4] *Equal contribution*
[*] *knut.drescher@unibas.ch*

This supplement published with The Optical Society on 14 May 2021 by The Authors under the terms of the Creative Commons Attribution 4.0 License in the format provided by the authors and unedited. Further distribution of this work must maintain attribution to the author(s) and the published article's title, journal citation, and DOI.

Supplement DOI: https://doi.org/10.6084/m9.figshare.14450286

Parent Article DOI: https://doi.org/10.1364/BOE.420788

# Single-objective high-resolution confocal light sheet fluorescence microscopy for standard biological sample geometries: supplemental document

## S1: Alignment of the optical system

Here we describe the main steps we follow in order to align the optical system (see Fig. 1B) using the nanohole array targets. We assume that all other optics are already pre-aligned and the protocol described below lists the final steps to obtain a fine-tuned, largely aberration-free image:

1. Position the prism holding the nanohole array in the O1 space and immerse it in the objective immersion liquid. Make sure to use an appropriate coverslip for the objective (thickness #1.5 in our case), and set the objective correction collar to an appropriate value (this is just the initial value - it must be fine-tuned along with setting of the correction collar of O2). Here, we illuminated the prism with conventional transmitted brightfield illumination so that the image contrast is based on the absorption and transmission of the light by the chromium layer.
2. Adjust the FP of O1 to be on the top surface of the coverslip so that you can see the glass-oil interface.
3. Position the prism in the center of the FOV and adjust the prism edge to coincide with the center of the objective, where the optical aberrations are minimal. We use a cross-hair in the eyepiece to move the prism edge to one of the central lines of the cross-hair, corresponding to the center of the objective O1 space.
4. For the following alignment steps, we changed the illumination from the transmitted brightfield LED that is inbuilt into the microscope body to a white light LED with a flexible gooseneck mount. With this LED, we illuminated the hypotenuse surface of the prism at an angle of approximately 45°. In this illumination geometry, the light hits the back side of the nanohole array and the incoming light shines through the prism glass towards the target and the oil. In this configuration, the aberrations are minimized as the refractive indexes in O1 and O2 match. The image contrast results from the light scattered at the nanoholes.
5. The side wall of the prism (where the nanohole pattern is) needs to be oriented such that when the resulting intermediate image reaches the O2 space it has the correct orientation to be reflected properly by the 45° mirror (see M5 on Fig. 1B and Fig. S5). Either the left or right side of the intermediate image plane needs to face the M5 mirror. The correct orientation can be tested by drawing a ray tracing diagram or by trial and error.
6. Next, the nanohole array pattern needs to be found and brought into focus in the FOV. For this, the XY stage needs to be moved so that the edge of the prism moves parallel to the central cross-hair line. Position it as close to the center of O1 as possible. By going upwards or downwards along *z* one can spot holes of the array that are in the FP, indicating that the array has been found. In our case, we also inscribed marks on the bottom (horizontal) surface of the prism, below the nanohole array, to facilitate the finding of the pattern.
7. Insert the M5 mirror in the space of O2 objective. If the objective uses immersion oil different from the refractive index of glass, you need to put a glass slide on top of the objective as well. Then immerse the mirror in the oil and set the initial correction collar value to the thickness of the glass slide (later you will need to fine tune the correction collar setting). Note that the M5 orientation must be such that it reflects the correct side of the intermediate image and be at 45° to the *z* direction of O2. In our case, we used D-shaped mirror and custom-made holder, which holds the mirror at 45° to the optical axis of O2. We mounted this holder on a small goniometer, which allowed to vary the angle ±10° in the vertical plane. This degree of freedom (polar angle) is critical to have in order to obtain proper alignment and thus minimize aberration. Not having this degree of freedom will result in the final image being fuzzy or not in focus throughout the FOV. The M5 mirror must also have a horizontal rotational degree of freedom so that the mirror's azimuth angle can be fine-tuned in the *xy* plane of O2. The rotational degree of freedom is also important in order to reduce the aberrations. The M5 mirror also requires *xy* and *z* translation degrees of freedom, which will be used in later steps of this alignment protocol. The *z* movement can also be achieved by moving objective O2 along *z*.

8. At this point we assume the prism with the nanohole array is properly aligned in the O1 space and that M5 mirror is inserted in the O2 space, and that the correction collars are set to the appropriate values.
9. Next, the M5 mirror needs to be positioned such that you observe the edge of the D-shaped mirror in the *xy* plane of the O2 objective. The observation is done in the O2-TL4 beam path by either a camera or an eye (using your eye and eyepiece for the initial alignment is much easier). After the mirror edge was found, you need to bring it in the center of the FOV and make sure the azimuth angle of M5 is oriented properly, *i.e.* you need to rotate M5 in the azimuth plane until the edge of the mirror is co-linear with the cross-hair of O2. For this to work, you need to align both cross-hairs of O1 and O2, to coincide with each other. Also, prior to this, you need to make sure that the cross-hair of O1 is co-linear with the light sheet plane (which will guarantee that the illumination and detection planes match).
10. The next step is to position the M5 mirror along *z* such that you can see the intermediate vertical plane, *i.e.* the image of the pattern (which the mirror M5 transforms to a horizontal image). Then you can move the mirror along *x* or *y* to cover *z* and thus see the whole pattern in the FOV of the camera/eye. Adjustments along *z* in O1 space might be also necessary in order to bring the pattern in the center of the FOV of O2 (as seen in O2-TL4 beam path). Note that these adjustments also imply that you need *xy* and *z* translation degrees of freedom to be able to align M5.
11. The next alignment steps are iterative. The system will be aligned when one obtains an aberration-free and distortion-free image of the nanohole array pattern. Most likely, the initial image of the pattern will be very skewed and distorted. The most important parameter to tune initially is the O2-TL2 distance - it influences greatly the distortion along Z, *e.g.* causing the bottom of the image to have a larger zoom than the upper part (or *vice versa*). You need to tune this distance so that the zoom is uniform throughout the FOV. Another important parameter to play with is TL1-TL2 distance. Although this distance is less important than O2-TL2 it can improve the image. The next important parameter to adjust is the polar angle of the M5 mirror - if you see that the focusing differs when you go up or down in *z* with the O2 objective, then you need to readjust this parameter. Other very important parameters are the correction collars of O1 and O2 - if nothing else can improve the image these parameters must be tuned. The last two important parameters to tune are the tip/tilt of the two mirrors M3 and M4 in between TL1-TL2 These parameters need to be iteratively adjusted to get a good image.
12. The next step is to replace the nanohole array target by a real sample in the O1 space and adjust the collar of the O1 objective for the given refractive index such that the image on the camera is as good as possible. When there is a refractive index mismatch between O1 space and O2 space, the useful *z*-range over which a high-quality image can be obtained will decrease, because although the correction collar can compensate aberrations substantially, it is not possible to reduce the aberrations completely. In addition, slight readjustment of the pair of mirrors M3 and M4 between TL1-TL2 can be helpful to obtain a well-compensated aberration-free image. At the edge of the field of view (*i.e.* more than ~30 µm away from the center), some aberrations are observable, which can manifest as barrel distortions.
13. The final step of the alignment is to synchronize the scanning light sheet (the galvo scanning) with the rolling shutter mode of the camera (the moving virtual confocal slit). This is explained in detail in Appendix E.

In a situation where the alignment could not be improved beyond certain point (*e.g.* remaining spherical aberrations along the *z* direction, elongated PSFs of nanoholes), a helpful trick can be to exchange the order of the objectives - e.g. O1 goes on the O2 place, and O2 on the O1 place. Although the specifications of the microscopy objectives are the same, in reality there might be a slight variability from objective to objective so that two objectives that are nominally identical can have a different magnitude of the aberrations. This is not noticed in normal single-objective microscopy, but when paired in setups as in APOM, such objective-to-objective variability can be noticed because the sensitivity to aberrations in APOM is greater than in normal horizontal imaging. Please note that to detect the APOM image, the rays must pass through more optical components and the image of the sample itself undergoes at least three transformation process: the sample is imaged by O1, image relayed to O2 (reimaged in O2 space), and finally the intermediate image in O2 is detected by O2-TL4. Therefore, if the mutual compensation is not good, it can lead to an increase of the aberrations. Changing the order of the two objectives can improve the aberration compensation in practice.

Another useful trick to circumvent the above-mentioned problem (dependence of image quality on the order of the objectives in the pair) is to slightly shift the detection camera away from the focal plane (optimal position is found by trial and error, in our case ca. +4 cm away from the focal plane gave good results). This

is equivalent to introducing a defocus aberration, which is a first-order spherical aberration. Hence, if it happens to have the opposite sign, it can in practice compensate in a very good way the not-optimally compensated spherical aberrations due to the O1-O2 pair.

## S2: Nanohole array target fabrication

The nanohole array is used for calibration purposes and to align the DC-APOM system so that the aberration and distortions are minimized when the vertical image is transformed into a horizontal image. Note that such beam path alignment can take significant effort and time for non-trained users, and the availability of a high-quality targets is critical. The nanohole array is shown in Fig. 1D.

The nanohole array was fabricated using a focused ion beam (FIB) in-house at the Materials Science Center, Philipps-Universität Marburg, by first depositing a 160 nm chromium layer (OD = 2.7) on a knife-edge prism (KRPB-10-10H, OptoSigma). The nanohole array pattern was then milled near the bottom edge of the prism (≈10 µm from the edge). The pattern consists of a square array of holes with 400 nm diameter and hole-to-hole distance of 7 µm, over an area of 70 x 70 $\mu m^2$. Other features, such as lines and text were added to facilitate alignment and calibration. The knife-edge prism was chosen as the holder for the nanohole arrays so that the pattern could be inscribed on a high quality flat optical glass surface, and because the prism ensures that the pattern naturally stays up-right vertical at 90° with respect to the focal plane of the objective O1. An important feature of the knife-edge prism is that it does not have a protection bevel on the knife-edge similar to other 90° prisms. This makes it possible to inscribe a pattern close to the bottom of the prism so that it is within the working distance of a high-NA microscope objective. Conventional 90° prisms, due to their safety bevel (ca. 100 – 200 µm), do not allow this.

## S3: Generating Gaussian and Bessel beams

As shown in the beam path (Fig. 1B), the amplitude mask GBM (Gaussian-Bessel mask) is used to shape the incoming collimated laser beam into two types of beam profiles - Gaussian or Bessel ones. The shape and the dimensions of the given beam defines, after focusing by the objective, the length and thickness of the generated light sheet in the *xyz*-space of the sample. The GBM mask design is shown in Fig. S1. The GBM mask consists of a patterned chromium layer (optical density OD = 3) in which an array of holes and rings with different sizes were etched (JD Photo Data, UK). By moving a different hole/ring into the beam path, a different beam shape is generated. The first column defines Gaussian (or Top-Hat) like beams, while the rest of the columns form mixture of Gaussian-Bessel beam modes. At a fixed ring diameter, a thinner ring results in a more tightly focused beam (thinner light sheet, stronger Bessel shape) and a longer light sheet (see Table S1). On the other hand, at a fixed ring thickness, increasing the diameter of a ring makes it more tightly focused (thinner light sheet) and shortens the length of the light sheet. Hence, one can choose the combination of outer and inner ring diameters that results in a beam shape that is best suited for a given application. Note also that although the Bessel beam gives thinner and longer light sheets compared with Gaussian beams, Bessel beams have more energy distributed in the side lobes of the resulting light sheet, resulting in more photobleaching in parts of the sample that are not imaged, which is undesirable. The increased energy in the beam side lobes will also increase the background of the signal as wider area from the sample is illuminated, and hence more scattering is to be expected. When Bessel beam profile is employed, it is therefore best to use a confocal slit (as used in the DC-APOM technique), which will cut this out-of-focus light resulting in a higher contrast and resolution of the acquired image. Another advantage of a Bessel beam compared to a Gaussian one is that Bessel beams fall in the class of beams which exhibit the so-called self-healing or self-reconstructing effect. This leads to an increased penetration depth of the beam inside the sample, which is especially useful for highly packed samples where scattering is an issue, such as bacterial biofilms or tissues.

A theoretical calculation of the light sheet dimensions resulting from focusing Gaussian, truncated Gaussian, and Bessel beams is provided in Appendix G.

Experimentally measured light sheet properties for the 100x/1.35 NA silicon oil objective and 488 nm illumination light are listed in Table S1 for each of the GBM mask holes and rings. A comparison of these

experimental light sheet properties with theory, which is described below, is shown in Fig. S2. These measurements were performed by measuring the reflection of the light sheet from a gold-coated glass slide (note that since the light sheet is vertical it falls normally on the interface). Using this experimental arrangement, the width of the light sheet was measured by positioning the center of the light sheet (where the intensity is at the maximum) on the gold-coated interface and estimating the full width at half maximum (FWHM) of the cross-section diameter of the reflected image (detected by the sCMOS camera). The length of the light sheet was measured by estimating the -*z* to +*z* distance (*i.e.* confocal parameter or twice the Rayleigh length) from the center of the light sheet where the intensity falls off to 50% of the maximum value. At this point the area of the beam increases twice in diameter compared to the center of the light sheet, as the waist of the light sheet is $\sqrt{2}\, w_0$ (where $w_0$ is the waist in the center of the light sheet). Note that when measuring the light sheet length with the microscope objective, the real length is twice the measured *z*-range since for a given change $\Delta z$ of the objective, the light travels twice this range (before and after reflection) before again reaching the focal plane where it is detected. An example of measured light sheets can be seen in Fig. S6 (in Widefield reflection mode).

## S4: Hardware and software control

For the control of the DC-APOM setup we used a Matlab GUI and Micro-Manager [1,2] *via* its Java binding to interact with hardware components, which have dedicated device driver support. Matlab was used to control the image acquisition process *via* Micro-Manager. Various settings of the devices (camera, laser power, etc.) were set directly in Micro-Manager, while others were set through the Matlab GUI. The processing of the data and images were also done in Matlab. For the standard widefield imaging, the Nikon NIS-Elements software was used, *e.g.* to measure the *xy* resolution based on fluorescent beads, or to position the nanohole array in O1 space.

A block diagram of the software control for 3D image stack acquisition is shown in Fig. S7C. The respective hardware communication and timing schemes are shown in Figure **S7:** S7A, B. Upon the start of a 3D image stack acquisition (step "Start 3D Stack Acquisition" in Fig. S7C) the Matlab GUI performs several initialization steps (moving the XY stage and the galvo *x* to their respective positions) and checks, and then sends a signal to the camera (sCMOS Zyla 4.2 PLUS, Andor) *via* the USB connection to start the frame acquisition. The camera acts as a master clock and sends control signals through the NI-DAQ card to turn the laser on, and to trigger the galvo to start scanning. The hardware timing scheme (Fig. S7B) shows the precise timing of the events. The AUX OUT 2 output of the camera is set to the "Exposed Row Clock" so that it sends a TTL pulse on each newly activated row of pixels, which indicates the start of the exposure for the given row. This camera output is connected to one of the NI-DAQ input ports, and the signal is processed so that on each new TTL Exposed Row Clock pulse, the voltage output level applied on the galvo is increased by a given step. Since this is quite a fast process and the galvo input acts as a low pass filter, the resulting voltage on the galvo is a smooth linear ramp from a given initial voltage $U_{min}$ to a given end voltage $U_{max}$. The voltage waveform on the galvo is a saw-tooth like pulse train. After the end of each scan (*i.e.* end of the frame exposure period), the galvo waits in its last position ("Rest") until a new control signal arrives for the new frame. In between the rest period, the camera transfers the acquired data to the workstation computer. After the Matlab GUI processed this frame, it directs the motorized stage to move by one $\Delta y$ step, and then starts a new acquisition frame until the whole 3D stack is acquired. At the end of each "Exposure" period, the laser is turned off until the beginning of the next frame to avoid unnecessary photobleaching of the sample. The laser source is synchronized with the TTL AUX OUT port of the camera. As we rely on a software mechanism to control the stage *via* the USB connection, this control mechanism is not optimal in terms of acquisition speed. A faster, but technically more challenging, control of the motorized stage would be *via* the NI card and the respective camera outputs as it was done for the galvo and the laser.

The principle of operation of the rolling shutter mode of the camera is shown on Figure **S8:** S8. This mode of the sCMOS camera is employed in order to form a (virtual) confocal slit [3], which creates the confocal effect needed to cut away the out-of-focus light and thereby reduce the background signal, which in turn increases the contrast and the resolution of the system. The principle of operation of the sCMOS camera rolling shutter and the respective virtual slit is the following:

1. The initial position of the virtual slit with respect to the image sensor before the beginning of the scanning is shown on Fig. S8A. The virtual slits on both sides of the sensor show the start and end position of the virtual slit and the occupied space in terms of pixels, *i.e.* one can think about the image sensor as an extended virtual sensor that includes the start and end position of the slit. The usable part of the image sensor in this acquisition mode is shown in gray. To illustrate the acquisition process, an image of a sample is shown as well. Note that the size of the virtual slit (width in terms of pixel rows) can be set in the software and therefore we consider the image sensor having additional imaginary pixel rows before the first and after the last usable pixel rows. This assumption is necessary in order for the electronics of the camera to output the correct number of TTL Exposed Row Clock pulses (the overall count will be defined by the slit width and the width of the sensor in pixels) so that the slit moves throughout from its initial position until its end position.
2. Prior to the beginning of the scanning, the Matlab GUI moves the galvo to the initial position so that the laser beam is located in the middle of the slit (see the blue dotted line on the Fig. S8A). This laser beam is synchronized with the movement of the slit so that it is always in the middle of the virtual slit during scanning. Below, more information is provided for how to initially position the laser beam so that the slit and the beam stay synchronized during the acquisition.
3. The position of the virtual slit right after the beginning of the scanning is shown on Fig. S8B. Here the slit has already moved along the direction of the scanning (indicated by the dark red arrow) by one pixel row. The dark red outline shows the new position of the slit with respect to the image sensor. Note that all drawn pixel rows outside the image sensor (i.e. outside the gray area) are not active pixels and are just drawn here for illustrating the principles of operation of the rolling shutter mode and the virtual confocal slit.
4. The shift of the slit with one pixel row to the right is communicated to the external devices with the help of one of the camera auxiliary output AUX OUT 2 (set to "TTL Exposed Row Clock"): Whenever a new pixel row is activated, it produces a new TTL output pulse rise, which goes into the NI-DAQ card and causes the card to raise the voltage level on the galvo input with a given value (in practice, on every new TTL Exposed Row Clock pulse, the NI-DAQ card reads the next voltage level from a list of predefined voltages that is set between $U_{min}$ and $U_{max}$).
5. During the scanning, the slit moves from one side of the image sensor to the other (see Fig. S8C). The direction of the movement can be controlled – the Andor Zyla 4.2 PLUS camera allows several modes of operation, two of them are suitable for controlling the virtual slit direction ("Bottom Up Sequential" or "Top Down Sequential"). The speed of the slit movement is set by the line scan speed and can be controlled within a given range. In Micro-Manager, this parameter is called "Andor sCMOS Camera-LightScanPlus-LineScanSpeed [lines/sec]". The line speed also defines the exposure time per pixel with respect to the laser beam, *i.e.* the dwell time that the center of the laser beam (the blue dotted line in Fig. S8) will spend in a given pixel row. Note that the overall exposure of a given pixel row is defined by the line speed and the slit width (Line-Speed x Slit-Width). This is the dwell time the pixel is actively exposed before the start of the readout by the electronics of the camera. Thus, the movement of the slit is due to a subsequent activation of a row (row start exposure) in front of the slit and simultaneously on the back of the slit a row becomes inactive (row readout). The active pixels are therefore defined only by the slit width (detection window height): at any given time, all sensor pixels outside of the slit region are not active and do not contribute to the image formation.
6. At the end of the scanning, the slit reaches the end position (see Fig. S8D) and the transfer of data to the workstation computer begins. If a new frame is to be acquired, the whole processed described above is repeated until all frames from a given 3D image stack are acquired.

Fig. S9 shows the most important camera settings that control the scanning process (in the "Device Property Browser" of the Micro-Manager software). The role and the meaning of the following parameters is worth mentioning:

1. "Andor sCMOS Camera-AuxiliaryOutSource (TTL I/O)" = "FireAny". This parameter controls the type of event to indicate (RowClock/FrameClock etc) on the AUX OUT I/O port of the camera. The current parameter value tells the camera to send a TTL pulse on the first AUX output when any row within a frame is being exposed (TTL level high during a frame). It is used in the setup to turn ON/OFF the laser source.

2. “Andor sCMOS Camera-AuxiliaryOutTwoSource (TTL I/O)” = “ExposedRowClock”. This parameter controls the type of event to indicate (RowClock/FrameClock etc) on the second AUX OUT 2 I/O port of the camera. The current value tells the camera to send a TTL pulse on the second AUX output when any new row has been activated (start row exposure). The duration of the TTL pulse is equal to the readout time and the frequency of the pulses indicates the speed of the slit. It is used in our setup to synchronize the galvo (light sheet) speed with the slit speed.
3. “Andor sCMOS Camera-LightScanPlus-AlternatingReadoutDirection” = “Off”. This option (also called Cyclemax) controls if the sensor alters the readout direction for each consecutive frame in a kinetic series (similar to bi-directional scanning). In the present case, it was turned off.
4. “Andor sCMOS Camera-LightScanPlus-ExposedPixelHeight” = “1.000”. This parameter controls the slit width in terms of number of active rows, and is set to 1000 pixels. As a rule of thumb - one usually sets this parameter to be equal the FWHM of the light sheet width (for optimal SNR and contrast).
5. “Andor sCMOS Camera-LightScanPlus-LineScanSpeed [lines/sec]” = “10.000”. This parameter controls the line speed of the rolling shutter or the sweeping speed of the virtual slit across the image sensor. This will also define the dwell time of the center of the laser beam (light sheet). If a stronger fluorescence signal is needed, a slower line speed must be set.
6. “Andor sCMOS Camera-LightScanPlus-ScanSpeedControlEnable” = “On”. This parameter is very important and must be set to “On” in order to activate the “LightScanPlus” capabilities of the camera and be able to control and adjust the other “LightScanPlus” parameters (otherwise the virtual confocal slit scanning will not work).
7. “Andor sCMOS Camera-LightScanPlus-SensorReadoutMode” = “Bottom Up Sequential”. This parameter controls the readout mode, which in turn controls the direction of virtual slit. At least two modes are possible - sweep from the bottom to the top of the sensor (“Bottom Up Sequential”) and from the top to the bottom of the sensor (“Top Down Sequential”).

A very important calibration procedure in DC-APOM is to set the center of the light sheet to coincide (and stay in sync) with the center of the virtual slit throughout the scanning process. In the present case, this was achieved by tuning the offset voltage $U_{offset}$ of the galvo, which defines the center of the scanned field of view (FOV), as well as the voltages ($U_{min}$ and $U_{max}$), which control the lower and the upper boundary of the scanned FOV. Ideally, the galvo's FOV and the camera FOV must coincide as well as the speed of the virtual slit and the galvo speed. Then the laser beam and the galvo will be always in sync during the scanning. A rule of thumb for achieving good synchronization is the following: In order to position the light sheet into the center of the slit, one needs to adjust the offset voltage ($U_{offset}$) of the galvo so that during scanning the image looks sharp and in contrast throughout the field of view. Adjusting $U_{min}$ and $U_{max}$ can also help to improve the performance and in turn the synchronization. For this calibration, we usually use a real sample, for example a biofilm. In this case it is very easy to see if the scanning beam is not in sync with the virtual moving slit, because if the slit width is equal to the FWHM of the light sheet and if they are not in sync, the image contrast and quality decreases significantly. Note that for every new experiment, this procedure must be repeated as well as regularly checked (usually prior to each measurement session). In principle, a software algorithm could be developed to automatically perform this calibration in the future.

## S5: Calculating the size of Gaussian, truncated Gaussian (Top-Hat), and Bessel beams

To estimate the expected light sheet properties (thickness and length) resulting from the choice of particular combinations of rings and holes on the GBM Mask (Fig. S1), we derived theoretical predictions of the beam FWHM in the *xy*-direction (FWHMxy, *i.e.* thickness) and FWHM in the *z*-direction (FWHMz, *i.e.* length) of the resulting light sheet, as described below.

*FWHMxy and FWHMz of Gaussian beams:*
The propagation of a Gaussian beam is described by the following equations

$$w(z) = w_0\sqrt{1 + \left(\frac{z}{z_R}\right)^2}, \tag{11}$$

$$\theta_{beam} = \tan^{-1}\left(\frac{\lambda_0}{n\pi w_0}\right) \approx \frac{\lambda_0}{n\pi w_0}, \tag{12}$$

$$z_R = \frac{n\pi w_0^2}{\lambda_0}, \tag{13}$$

where $w(z)$ describes the evolution in size of the beam waist radius $w_0$ along the optical axis ($z$-direction), $w_0$ is the beam waist radius (at z = 0) at $1/e^2$ intensity level, $\theta_{beam}$ is the divergence of the beam (half of the angle of the full angular spread of the beam), $z_R$ is the Rayleigh length, $n$ is the refractive index of the medium where the propagation occurs, and $\lambda_0$ is the wavelength of the light in vacuum. Thus, a beam of radius $r_{beam}$ (at $1/e^2$) falling on the BFP of an objective with focal length $f_{obj}$ will have numerical aperture

$$NA_{beam} = \frac{r_{beam}}{f_{obj}} = n\sin\theta_{beam} \approx n\theta_{beam}. \tag{14}$$

Hence, substituting Eq. (14) into Eq. (12) we can find a formula for the beam waist radius in the focus as a function of the input beam parameters, i.e.

$$w_0 = \frac{\lambda_0}{\pi NA_{beam}}, \tag{15}$$

which is valid for $w_0 \gg \lambda_0$. Thus, we obtain an alternative expression for $z_R$,

$$z_R = \frac{n\lambda_0}{\pi NA_{beam}^2} = \frac{nw_0}{NA_{beam}}. \tag{16}$$

Based on these expressions for $w_0$ and $z_R$, we arrive at the beam width and length in the focal plane described in terms of FWHMxy and FWHMz:

$$FWHMxy = w_0\sqrt{2\ln(2)} \approx 1.18w_0 = \frac{1.18\lambda_0}{\pi NA_{beam}}, \tag{17}$$

$$FWHMz = 2z_R = \frac{2n\lambda_0}{\pi NA_{beam}^2}. \tag{18}$$

These equations are based on the assumption of paraxial beam propagation and on the assumption that the Gaussian beam is not truncated (or truncated at most up to a diameter of $2w_0$). For high-NA objectives, this is not always the case. In addition, some part of the incoming laser beam is blocked by the GBM mask (Fig. S1). In our DC-APOM system, we use a fixed incoming beam diameter of ≈7 mm, and smaller mask apertures cut more from the incoming beam. In order to more accurately predict the beam size, we assumed a truncated Gaussian beam below (see Fig. S2A for a comparison between Gaussian and truncated Gaussian beams).

*Scalar diffraction theory of truncated Gaussian (top-hat) and Bessel beams:*

Here we compute the light sheet size resulting from beam that is truncated by an aperture introduced in the optical beam path. Specifically, we consider a top-hat beam profile, i.e. a circular beam with constant intensity and phase profile throughout the defining aperture. If such a beam falls on the BFP of an objective, it results in intensity profile described by the well-known Airy disk in the *xy*-plane and the $\text{sinc}^2$ function in the

$z$-direction. However, here, for completeness we will consider the scalar Debye diffraction integral to include the case of Bessel beams as well.

Following a previously described approach [4], and with some adaptation for the case of a Bessel beam, we employ the scalar Debye integral to describe the amplitude distribution $h(r, z, k)$ of the electric field near the focal region of a high-NA objective [5],

$$\mathrm{h(r,z,k)} = \mathrm{C_0} \int_{\alpha_{id}}^{\alpha_{od}} \sqrt{\cos\theta}\, \mathrm{J_0(kr\sin\theta)}\, \mathrm{e^{-ikz\cos\theta}} \sin\theta\, \mathrm{d}\theta\ , \tag{19}$$

where $r = \sqrt{x^2 + y^2}$ , $z$ is the distance along the optical axis, $k = 2\pi n/\lambda_0$ is the wave number, $C_0$ is a complex constant, $\theta$ is the integration angle (the angle subtended by the optical axis and a point of interest on the objective lens, viewed from the focus of the objective), $\alpha_{in}$ and $\alpha_{od}$ are the half-angles of the inner and outer beam diameters of the ring-shaped beam as seen from the focal point (in between these angles the input beam has non-zero constant intensity and phase). The apodization term $\sqrt{\cos\theta}$ describes the phase change introduced in a plane wave falling on aplanatic objective lens. $J_0$ is the Bessel function of first kind, zeroth order.

As we have a centrosymmetric system, the above integral can be transformed into two simpler and separate integrals for the distribution of the amplitude: $h_r(r, k) = h(r, z = 0, k)$ in the focal plane, and $h_z(z, k) = h(r = 0, z, k)$ along the optical axis, *i.e.*

$$\mathrm{h_r(r,k)} = \mathrm{C_0} \int_{\alpha_{id}}^{\alpha_{od}} \sqrt{\cos\theta}\, \mathrm{J_0(kr\sin\theta)} \sin\theta\, \mathrm{d}\theta\ , \tag{20}$$

$$\mathrm{h_z(z,k)} = \mathrm{C_0} \int_{\alpha_{id}}^{\alpha_{od}} \sqrt{\cos\theta}\, \mathrm{e^{-ikz\cos\theta}} \sin\theta\, \mathrm{d}\theta\ . \tag{21}$$

To simplify the solution and without loss of precision for the present case, we can safely assume paraxial beam propagation (*i.e.* small angle $\theta$), and hence $\sqrt{\cos\theta} \approx 1$ in both integrals, but $\sin\theta \approx \theta$ only in $h_r(r, k)$. This assumption transforms the integrals into

$$\mathrm{h_r(r,k)} \approx \mathrm{C_0} \int_{\alpha_{id}}^{\alpha_{od}} \mathrm{J_0(kr\theta)\theta d\theta}\ , \tag{22}$$

$$\mathrm{h_z(z,k)} \approx \mathrm{C_0} \int_{\alpha_{id}}^{\alpha_{od}} \mathrm{e^{-ikz\cos\theta}} \sin\theta\, \mathrm{d}\theta\ . \tag{23}$$

These integrals have closed form analytical solutions. In terms of the intensity (normalized to max. value of one), $I_r(r, k) = |h_r(r, k)|^2$ and $I_z(z, k) = |h_z(z, k)|^2$, the integral solutions can be used to obtain

$$\mathrm{I_r(r,k)} = 4\left[\frac{\alpha_{od}\mathrm{J_1(kr\alpha_{od})} - \alpha_{id}\mathrm{J_1(kr\alpha_{id})}}{\mathrm{kr}(\alpha_{od}^2 - \alpha_{id}^2)}\right]^2\ , \tag{24}$$

$$\mathrm{I_z(z,k)} = \frac{2(1 - \cos(\mathrm{kz}[\cos\alpha_{id} - \cos\alpha_{od}]))}{[\mathrm{kz}(\cos\alpha_{id} - \cos\alpha_{od})]^2}\ . \tag{25}$$

This can be rewritten in the following more convenient form (substituting $\epsilon = \alpha_{id}^2/\alpha_{od}^2$):

$$I_r(r,k) = 4\left[\frac{J_1(kr\alpha_{od})-\sqrt{\epsilon}J_1(\sqrt{\epsilon}kr\alpha_{od})}{kr\alpha_{od}(1-\epsilon)}\right]^2 , \tag{26}$$

$$I_z(z,k) = \left[\mathrm{sinc}\left(\frac{kz}{2}[\cos\alpha_{id} - \cos\alpha_{od}]\right)\right]^2 . \tag{27}$$

For systems that obey the Abbe sine condition $NA_{id,od} = \frac{r_{id,od}}{f_{obj}}$, and noting that for small angles $NA_{id,od} = n\sin\alpha_{id,od} \approx n\alpha_{id,od}$, we obtain

$$\epsilon = \left(\frac{r_{id}}{r_{od}}\right)^2 = \left(\frac{NA_{id}}{NA_{od}}\right)^2 , \tag{28}$$

$$I_r(r,k_0) = 4\left[\frac{J_1(k_0 rNA_{od})-\sqrt{\epsilon}J_1(\sqrt{\epsilon}k_0 rNA_{od})}{k_0 rNA_{od}(1-\epsilon)}\right]^2 . \tag{29}$$

Along the *z*-direction we consider two cases. In the first case, we use the fact that

$$\alpha_{od,id} = \arcsin\left(\frac{NA_{od,id}}{n}\right) , \tag{30}$$

$$\cos\left(\arcsin\left(\frac{NA_{od,id}}{n}\right)\right) = \sqrt{1-\frac{NA_{od,id}^2}{n^2}} , \tag{31}$$

and hence

$$\cos\alpha_{id} - \cos\alpha_{od} = \frac{\sqrt{n^2-\epsilon NA_{od}^2}-\sqrt{n^2-NA_{od}^2}}{n} . \tag{32}$$

Thus, for $I_z(z,k_0)$ we obtain

$$I_z(z,k_0) = \left[\mathrm{sinc}\left(\frac{k_0 z}{2}\left[\sqrt{n^2-\epsilon NA_{od}^2}-\sqrt{n^2-NA_{od}^2}\right]\right)\right]^2 . \tag{33}$$

In the second case, in the equation for $I_z(z,k_0)$ we assume small angles, *i.e.*

$$\cos\alpha_{id} - \cos\alpha_{od} \approx \frac{(\alpha_{od}^2-\alpha_{id}^2)}{2} = \frac{NA_{od}^2}{2n^2}(1-\epsilon) , \tag{34}$$

and hence we obtain a simpler expression for $I_z(z,k_0)$, *i.e.*

$$I_z(z,k_0) = \left[\mathrm{sinc}\left(\frac{k_0 zNA_{od}^2}{4n}(1-\epsilon)\right)\right]^2 , \tag{35}$$

where $\epsilon$ is the square of the ratio of the inner $r_{id}$ over outer $r_{od}$ beam radius (or angles), $k_0 = 2\pi/\lambda_0$ is the wave number in vacuum, $NA_{id,od}$ are the inner and outer numerical aperture of the beam.

From here, we can derive the expressions for FWHM in the *xy*- and *z*-directions for truncated Gaussian as well as Bessel beams. In the case of a truncated Gaussian beam, the parameter $\epsilon = 0$ (*i.e.* $NA_{id} = 0$ and $NA_{od} = NA_{beam}$), and hence

$$\mathrm{I_r(r, k_0)} = 4\left[\frac{\mathrm{J_1(k_0 r NA_{beam})}}{\mathrm{k_0 r NA_{beam}}}\right]^2, \tag{36}$$

$$\mathrm{I_z(z, k_0)} = \left[\mathrm{sinc}\left(\frac{\mathrm{k_0 z}}{2}\left[\mathrm{n} - \sqrt{\mathrm{n^2 - NA_{beam}^2}}\right]\right)\right]^2, \tag{37}$$

or for small angles

$$\mathrm{I_z(z, k_0)} = \left[\mathrm{sinc}\left(\frac{\mathrm{k_0 z NA_{beam}^2}}{\mathrm{4n}}\right)\right]^2. \tag{38}$$

Thus, in the focal *xy*-plane, the intensity is described by the well-known Airy pattern with radius of the Airy disk $r_{Airy}$ (measured at zero intensity, *i.e.* when the argument $k_0 r NA_{beam} \approx 3.83$) and the FWHMxy is given by

$$\mathrm{r_{Airy}} = 0.61\frac{\lambda_0}{\mathrm{NA_{beam}}}, \tag{39}$$

$$\mathrm{FWHMxy} \approx 0.84\mathrm{r_{Airy}} \approx 0.51\frac{\lambda_0}{\mathrm{NA_{beam}}}. \tag{40}$$

Accordingly, along the *z*-direction, the radius $z_0$ (at zero intensity, *i.e.* when the argument of the sinc$^2$ is $\pi$) and FWHMz of the intensity pattern are given by

$$\mathrm{z_0} = \frac{\lambda_0}{\mathrm{n} - \sqrt{\mathrm{n^2 - NA_{beam}^2}}}, \tag{41}$$

or for small angles

$$\mathrm{z_0} = \frac{2\mathrm{n}\lambda_0}{\mathrm{NA_{beam}^2}}. \tag{42}$$

It can be shown that the FWHM along *z* of the sinc$^2$ function is at ca. 89% of the zero radius, *i.e.*

$$\mathrm{FWHMz} \approx 0.89\mathrm{z_0} = \frac{0.89\lambda_0}{\mathrm{n} - \sqrt{\mathrm{n^2 - NA_{beam}^2}}}, \tag{43}$$

or for small angles

$$\mathrm{FWHMz} \approx 0.89\mathrm{z_0} = \frac{1.78\mathrm{n}\lambda_0}{\mathrm{NA_{beam}^2}}. \tag{44}$$

Equations (40) and (44) are the predictions of the FWHMxy and FWHMz of the truncated Gaussian (top-hat) beams using scalar diffraction theory.

To compute the FWHMxy and FWHMz for a Bessel beam, we note that in the case of a Bessel beam, the parameter $\epsilon \neq 0$, and hence

$$\mathrm{I_r}(\mathrm{r}, \mathrm{k_0}) = 4\left[\frac{\mathrm{J_1}(\mathrm{k_0 r NA_{od}}) - \sqrt{\epsilon}\mathrm{J_1}(\sqrt{\epsilon}\mathrm{k_0 r NA_{od}})}{\mathrm{k_0 r NA_{od}}(1-\epsilon)}\right]^2, \tag{45}$$

$$\mathrm{I_z}(\mathrm{z}, \mathrm{k_0}) = \left[\mathrm{sinc}\left(\frac{\mathrm{k_0 z}}{2}\left[\sqrt{\mathrm{n}^2 - \epsilon\mathrm{NA_{od}^2}} - \sqrt{\mathrm{n}^2 - \mathrm{NA_{od}^2}}\right]\right)\right]^2, \tag{46}$$

or for small angles

$$\mathrm{I_z}(\mathrm{z}, \mathrm{k_0}) = \left[\mathrm{sinc}\left(\frac{\mathrm{k_0 z NA_{od}^2}}{4\mathrm{n}}(1-\epsilon)\right)\right]^2. \tag{47}$$

Finding the radius $r_0$ (at zero intensity) of the main lobe of the Bessel beam described by $I_r(r, k_0)$ above is not possible analytically. However, a compact expression for FWHMxy can be derived with the help of a Taylor series expansion (taking first three non-zero terms, and thus obtaining fourth degree polynomial) of $I_r(r, k_0)$ around $k_0 r NA_{od} = 0$ and solving for the FWHM level, *i.e.* $I_r(r, k_0) = 0.5$. This leads to the following closed form approximation, with relative error of 2-5%,

$$\mathrm{FWHMxy} = \frac{2\lambda_0}{\pi \mathrm{NA_{od}}}\bar{\epsilon}, \tag{48}$$

Where $\bar{\epsilon}$ is a parameter that depends on $\epsilon$ and has the following form

$$\bar{\epsilon} = \sqrt{\frac{6\epsilon + 6 - \sqrt{6\epsilon^2 + 24\epsilon + 6}}{5\epsilon^2 + 8\epsilon + 5}}. \tag{49}$$

Accordingly, along the *z*-direction, finding the radius $z_0$ at zero intensity and FWHMz of main lobe of the Bessel beam is straightforward (because the first zeros of the sinc$^2$ function are at $\pm\pi$), resulting in

$$\mathrm{z_0} = \frac{\lambda_0}{\sqrt{\mathrm{n}^2 - \epsilon\mathrm{NA_{od}^2}} - \sqrt{\mathrm{n}^2 - \mathrm{NA_{od}^2}}}, \tag{50}$$

or for small angles

$$\mathrm{z_0} = \frac{2\mathrm{n}\lambda_0}{\mathrm{NA_{od}^2}(1-\epsilon)}. \tag{51}$$

It can be shown that the FWHM along the *z*-direction of the sinc$^2$ function is at ca. 89% of the zero radius, *i.e.*

$$\mathrm{FWHMz} \approx 0.89\mathrm{z_0} = \frac{0.89\lambda_0}{\sqrt{\mathrm{n}^2 - \epsilon\mathrm{NA_{od}^2}} - \sqrt{\mathrm{n}^2 - \mathrm{NA_{od}^2}}}, \tag{52}$$

or for small angles

$$\mathrm{FWHMz} \approx 0.89\mathrm{z}_0 = \frac{1.78\mathrm{n}\lambda_0}{\mathrm{NA}_{\mathrm{od}}^2(1-\epsilon)}\,. \tag{53}$$

Equations (48) and (53) are the predictions of the FWHMxy and FWHMz of a Bessel beam. A comparison between experiment, approximated scalar Debye integral (paraxial theory) and the non-approximated scalar Debye integral (full theory) for FWHMxy and FWHMz is shown in Fig. S2. It shows that the approximation for the FWHMxy and FWHMz above can be used to predict the properties of the light sheets with good accuracy.

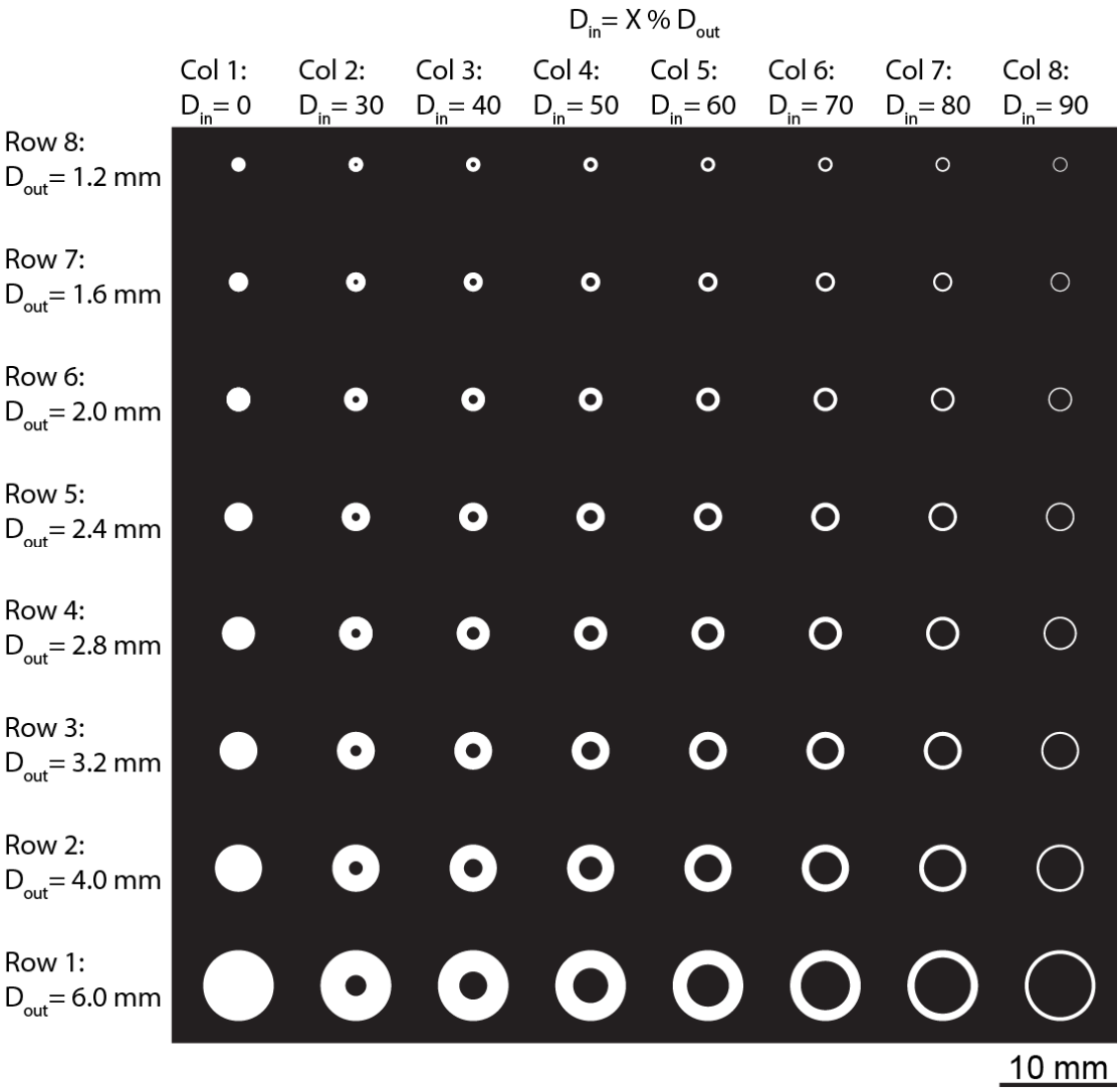


**Figure S1: Schematic diagram of the Gaussian-Bessel Mask (GBM) utilized in the optical system.** There are overall 8x8 positions with holes/rings with predefined outer ($D_{out}$) and inner ($D_{in}$) diameters. In this drawing, white color indicates transparent areas in the mask, and black color indicates the opaque chromium layer. For a given row, $D_{out}$ is constant, whereas $D_{in}$ changes in the range of 30% to 90% from $D_{out}$ (with a step of 10%). For a given column, $D_{in}$ is a constant percentage value of $D_{out}$. This GBM design enables the users to produce a broad range of light sheets with different beam thicknesses and lengths. The 100% transparent holes ($D_{in}$ = 0 mm) result in a Gaussian-like beam (when focused by the objective), while for the ring patterns, the resulting beam will be a mixture of a Gaussian and Bessel-like modes (the thinner the ring, the stronger the Bessel component of the beam).

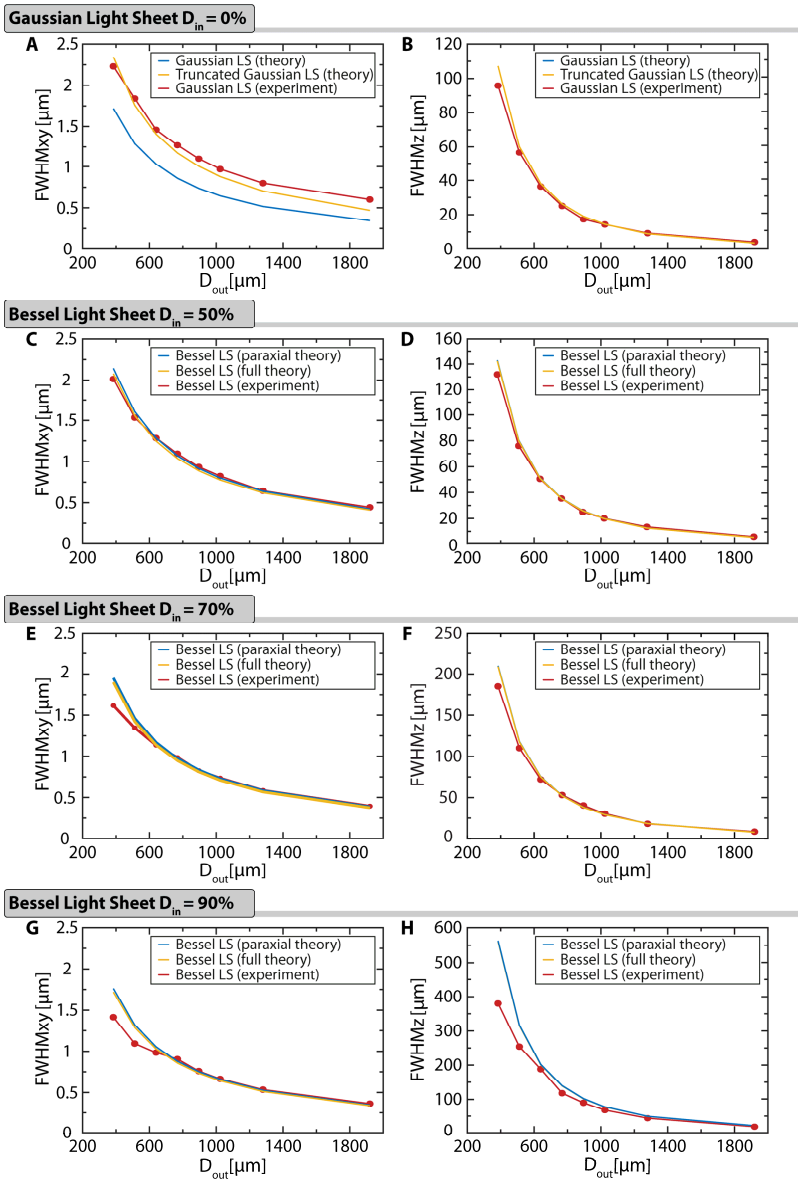


**Figure S2: Experimental and theoretical light sheet sizes for different Gaussian and Bessel beams.** The beams were shaped with the GBM mask, and the light sheet sizes (thickness: FWHMxy, length: FWHMz) are plotted as a function of the mask aperture size $D_{out}$ (outer beam/aperture diameter) and $D_{in}$ (inner beam/aperture diameter) on the back focal plane of the 100x/1.35 NA silicon oil objective (Olympus). Panels A and B represent measurements for a Gaussian light sheet ($D_{in}$ = 0 µm, see Fig. S1, Table S1). The blue curves are calculated according the Gaussian beam theory. The red curves assume a truncated Gaussian (TG) beam, *i.e.* a constant non-zero intensity and constant phase within the given aperture. Note that since the incoming beam overfills the GBM mask aperture, the measured FWHMxy and FWHMz (red curve with circles) are described best by assuming a TG beam (orange curve). Panels C, D, E, F, G, H represent measurements for Bessel light sheets for three values of $D_{in}$ (50%, 70% and 90% of $D_{out}$). Theoretical light sheet sizes calculated with the paraxial approximation of the scalar diffraction theory gave satisfactory accuracy for the estimation of the expected light sheet dimensions in significant part of the $D_{out}$ range. The discrepancy between experimental measurements and the paraxial theory at small beam diameters can be attributed to, *e.g.*, changes of the beam size due to diffraction, finite optical density of dark zones of the GBM mask, imperfect alignment, or variation in the magnification. The orange curves marked as "full theory" were calculated numerically using the full scalar diffraction integral, whereas the curves marked with "paraxial theory" were calculated using the paraxial approximation of the scalar diffraction integral. The red and blue/orange curves largely overlap.

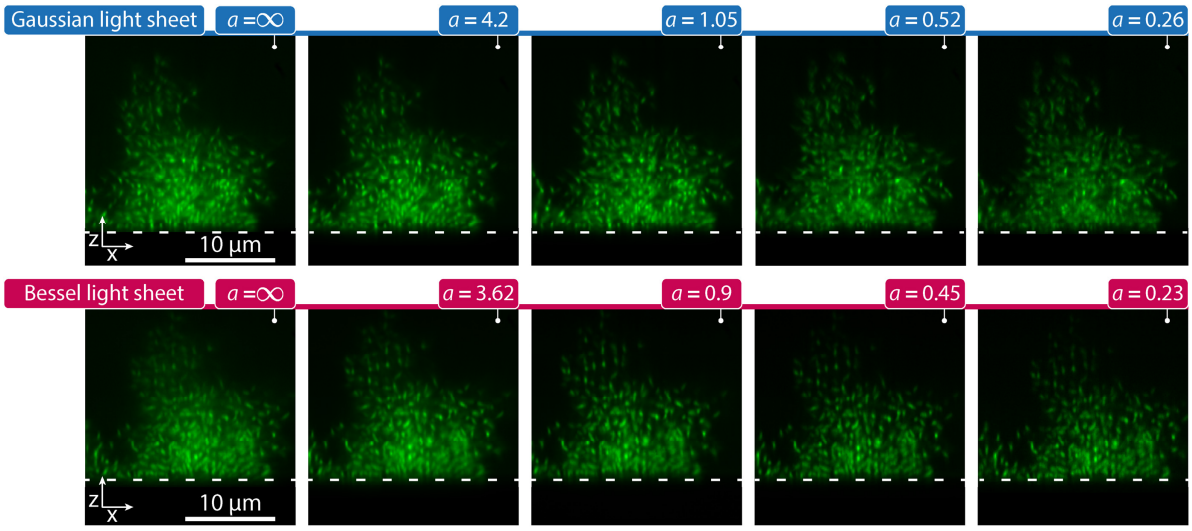


**Figure S3: Effect of the confocal slit size on DC-APOM image quality for bacterial biofilms.** Qualitative comparison of a stained and fixed *V. cholerae* biofilm imaged with different virtual confocal slit sizes using a Gaussian light sheet (size: FWHMxy = 2.231 µm, FWHMz = 96 µm) or a Bessel light sheet (size: FWHMxy = 1.154 µm, FWHMz = 31.4 µm). The ratio $a$ is defined as $a$ = confocal slit width/FWHMxy, and the value of a is listed above each panel. The dotted white lines in the microscope images denote the position of the glass coverslip to which the biofilm is firmly attached.

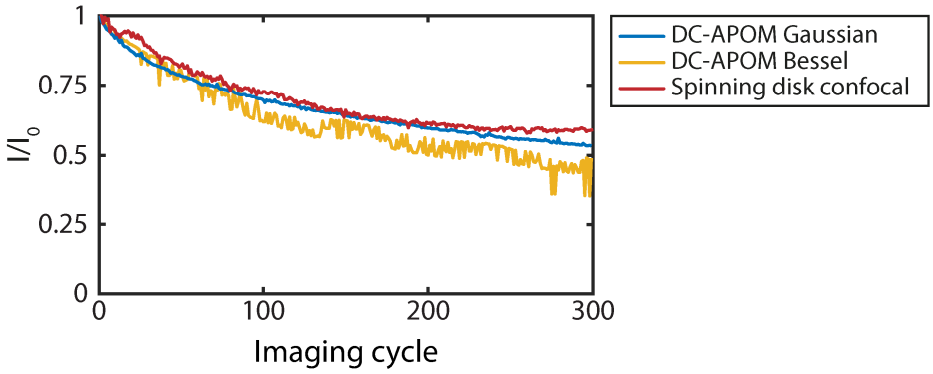


**Figure S4: Photobleaching control experiment.** The photobleaching performance for the acquisition of either a single horizontal plane (spinning disk confocal) or a single axial plane (DC-APOM) is compared in this control experiment. Here, the same light energy was deposited for all three imaging modalities. This results in similar photobleaching for all three imaging modalities. Photobleaching experiments were performed using biofilms that were stained with SYTO9 and fixed with formaldehyde. Photobleaching was measured as fluorescence intensity $I$ at a given imaging cycle number, normalized by the initial fluorescence intensity $I_0$.

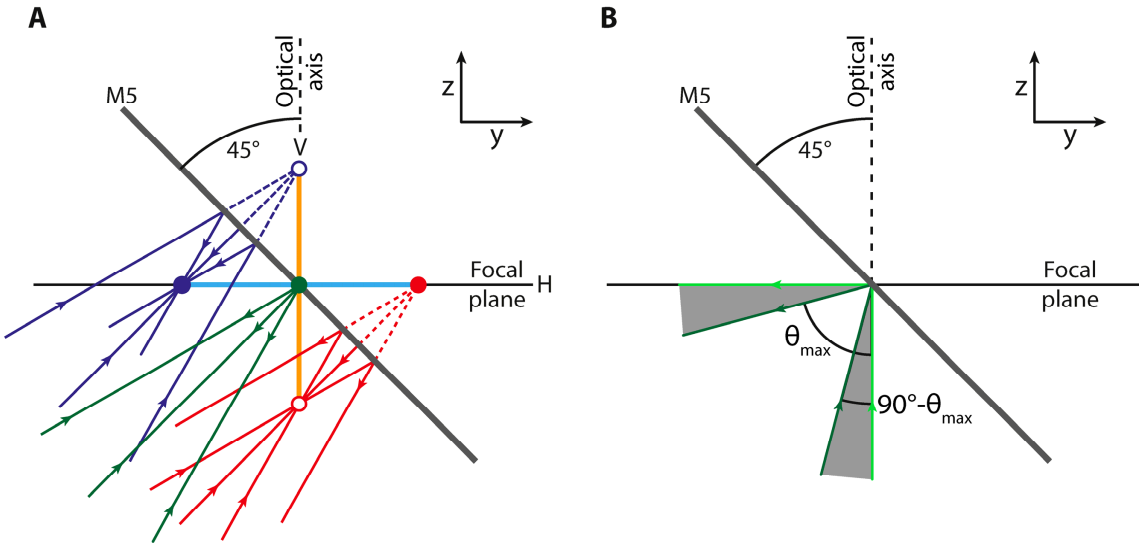


**Figure S5: Ray tracing diagram in the objective O2 space, illustrating the rotation from a vertical image to a horizontal image.** (**A**) Initially, the three open circles (purple, green red) represent an intermediate image of in the O2 space the object placed in the O1 space. The intermediate image is generated on the vertical plane V (orange). When the mirror M5 is introduced at 45° with respect to the optical axis, it alters the way in which the rays converge that come from objective O2 [6,7]. The purple rays converge on a point on the horizontal focal plane H (the purple filled circle). The green point already lies on the focal plane so that the rays simply switch the direction of propagation. The red rays initially converge to a point on V, but after reflection from M5 the rays propagate back to objective O2 and for the observer they will appear as if they emerged from the red filled circle on the focal plane (see the dotted red lines, which converge in the red filled circle). The presence of mirror M5 thus effectively transforms the vertical image from plane V to a horizontal image in the focal plane H. Note that because the detection now occurs in the focal plane of objective O2, the image of the vertical plane will be transmitted to the camera with minimum aberrations. (**B**) A loss of signal occurs during the image rotation due to the finite NA. This is illustrated by the ray bundle between the light green and dark green rays, which escapes the aperture of the objective O2.

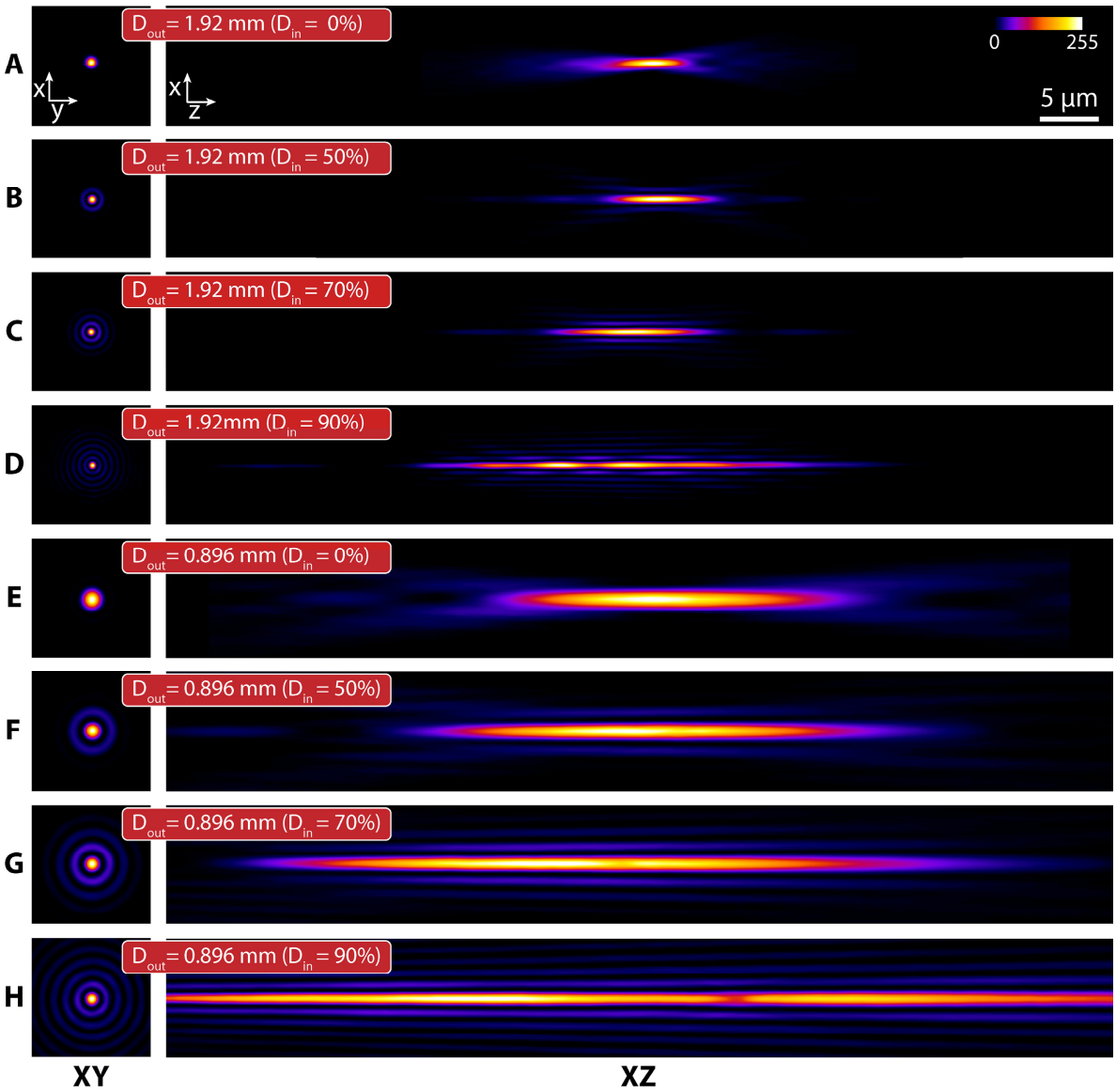


**Figure S6: Images of different beams that are scanned to form a light sheet, in the XY and XZ planes.** Panels A-H show the influence of the aperture (or beam) diameters $D_{out}$ (outer diameter in the back focal plane) and $D_{in}$ (inner diameter, as percentage of $D_{out}$) on the size of the light sheets. Images were obtained by scanning along the Z-axis of the objective and imaging the XY cross sections of the reflected 488 nm laser light from Au-coated glass slide. Each image was normalized to the maximum 8-bit pixel value of 255. In the Z-direction, the image was extended 2x to reflect that scan step of $\Delta z$ leads to the light sheet traveling $2\Delta z$. The XY and the XZ images are displayed using the same physical scale. In Panels A, B, C, D the beam was generated using the GBM for $D_{out}$ = 1.92 mm (at the back focal plane) and varying $D_{in}$ from 0% up to 90% of $D_{out}$. In Panels E, F, G, H the beam was generated using the GBM for $D_{out}$ = 0.896 mm (at the back focal plane) and varying $D_{in}$ from 0% up to 90% of $D_{out}$. Increasing the outer diameter $D_{out}$ results in more tightly focused beam (and vice versa) whereas increasing the $D_{in}$ (for a given $D_{out}$) leads to thinner beam, with increased length, but at the cost of more energy spread in the beam's side lobes. Note that beams with $D_{in}$ = 0% will be Gaussian-like, while increasing $D_{in}$ leads to more Bessel-like light sheets.

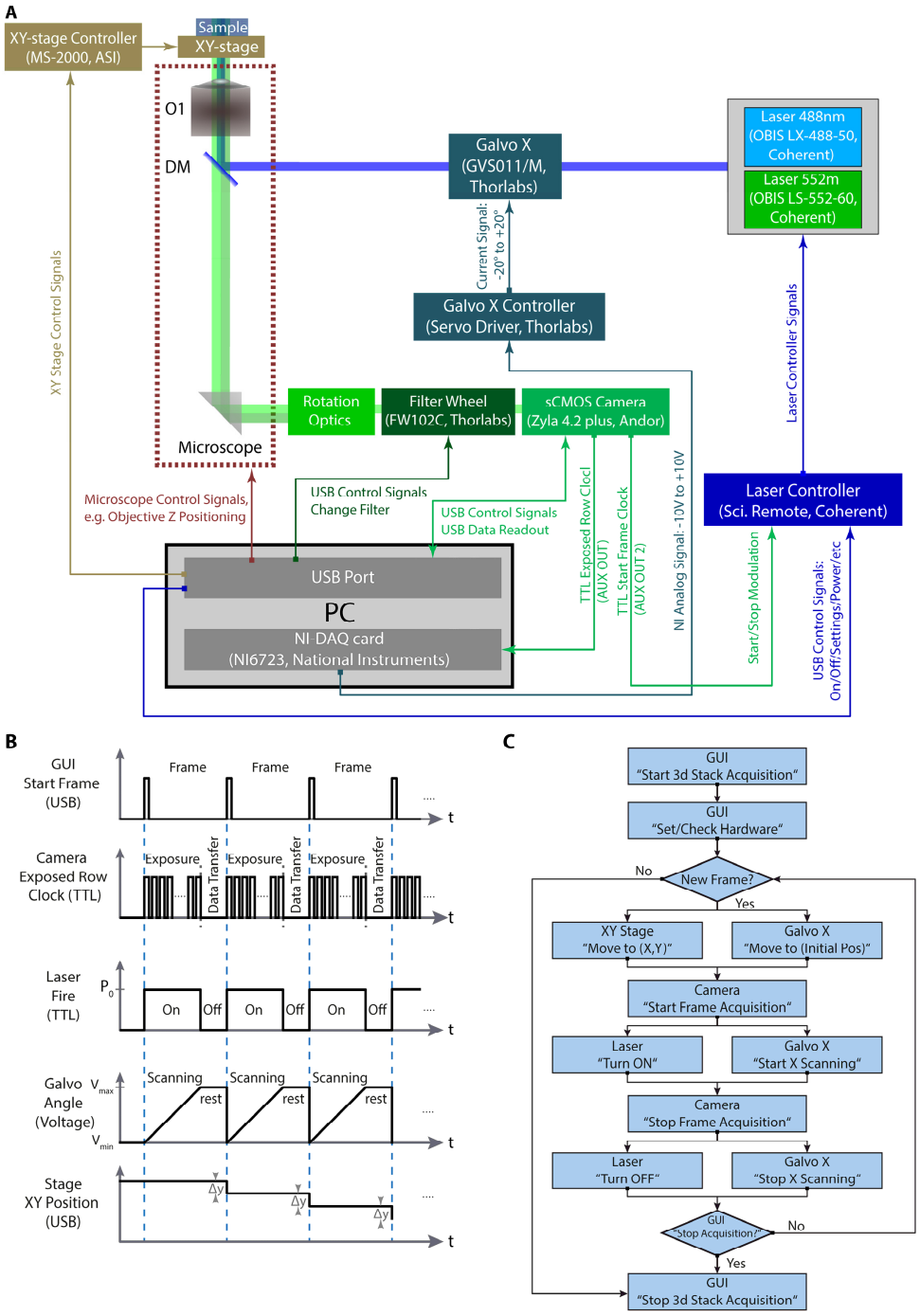


**Figure S7: Hardware communication scheme of the DC-APOM system.** (**A**) wiring of the main pieces of hardware. After the GUI-based control software sends the signal to the camera to start the acquisition, the camera sends control TTL signals to the NI-DAQ card, which then drives the galvo and the laser. The motorized XY stage is controlled by the GUI-based software. After the end of each acquisition frame, the XY stage is move to the new position. Further details about the hardware communication is are provided in Appendix E. (**B**) Hardware timing scheme and (**C**) software block diagram.

**Figure S8: Illustration of the virtual confocal slit generated using the rolling shutter mode of the camera.** The virtual confocal slit is indicated by the red box. (**A**) The position of the virtual slit is indicated before the start of a scan. (**B**) Position of the virtual slit right after the start of a scan. The slit moves one pixel row at a time. (**C**) Position of the slit during scanning. (**D**) Position of the virtual slit at the end of a scan.

| Property | Value |
|---|---|
| Andor sCMOS Camera-AccumulateCount | 1 |
| Andor sCMOS Camera-AcquisitionWindow | Custom AOI (2048x2048) |
| Andor sCMOS Camera-AuxiliaryOutSource (TTL I/O) | FireAny |
| Andor sCMOS Camera-AuxiliaryOutTwoSource (TTL I/O) | ExposedRowClock |
| Andor sCMOS Camera-Binning | 1x1 |
| Andor sCMOS Camera-CameraFirmware | 15.8.12.0 |
| Andor sCMOS Camera-CameraID | VSC-05777 |
| Andor sCMOS Camera-CameraModel | ZYLA-4.2P-USB3 |
| Andor sCMOS Camera-CameraName | Zyla 4.2 USB3 |
| Andor sCMOS Camera-CurrentSoftware | 3.12.30003.0 |
| Andor sCMOS Camera-Description | SDK3 Device Adapter for sCMOS cameras |
| Andor sCMOS Camera-ElectronicShutteringMode | Rolling |
| Andor sCMOS Camera-Exposure | 100 |
| Andor sCMOS Camera-Ext (Exp) Trigger Timeout[ms] | 10.000 |
| Andor sCMOS Camera-FanSpeed | On |
| Andor sCMOS Camera-FrameRate | 0,0285 |
| Andor sCMOS Camera-FrameRateLimits | Min: 0.00000 Max: 3.27547 Max Sustain: 39.31927 |
| Andor sCMOS Camera-LightScanPlus-AlternatingReadoutDirecti... | Off |
| Andor sCMOS Camera-LightScanPlus-ExposedPixelHeight | 1.000 |
| Andor sCMOS Camera-LightScanPlus-ExternalTriggerDelay [s] | 0 |
| Andor sCMOS Camera-LightScanPlus-LineScanSpeed [lines/sec] | 10.000 |
| Andor sCMOS Camera-LightScanPlus-RowReadTime | 0,0001 |
| Andor sCMOS Camera-LightScanPlus-ScanSpeedControlEnable | On |
| Andor sCMOS Camera-LightScanPlus-SensorReadoutMode | Bottom Up Sequential |
| Andor sCMOS Camera-Overlap | Off |
| Andor sCMOS Camera-PixelEncoding | Mono16 |
| Andor sCMOS Camera-PixelReadoutRate | 200 MHz - lowest noise |
| Andor sCMOS Camera-RollingShutterGlobalClear | Off |
| Andor sCMOS Camera-Sensitivity/DynamicRange | 16-bit (low noise & high well capacity) |
| Andor sCMOS Camera-SensorCooling | On |
| Andor sCMOS Camera-SensorTemperature | -0,44 |
| Andor sCMOS Camera-ShutterOutputMode | Closed |
| Andor sCMOS Camera-ShutterTransferTime [s] | 0 |
| Andor sCMOS Camera-SpuriousNoiseFilter | On |
| Andor sCMOS Camera-StaticBlemishCorrection | On |
| Andor sCMOS Camera-TemperatureControl | 0.00 |
| Andor sCMOS Camera-TemperatureStatus | Stabilised |
| Andor sCMOS Camera-TransposeCorrection | 0 |
| Andor sCMOS Camera-TransposeMirrorX | 0 |
| Andor sCMOS Camera-TransposeMirrorY | 0 |
| Andor sCMOS Camera-TransposeXY | 0 |
| Andor sCMOS Camera-TriggerMode | Internal (Recommended for fast acquisitions) |

**Figure S9: Camera settings in the Micro-Manager software.** The parameters enclosed in red boxes show the settings that are important for the control of the virtual confocal slit scanning and for synchronization of other hardware.

| | | $D_{in}$ | | | | | | | |
|---|---|---|---|---|---|---|---|---|---|
| | | **Col 1 (0%)** | **Col 2 (30%)** | **Col 3 (40%)** | **Col 4 (50%)** | **Col 5 (60%)** | **Col 6 (70%)** | **Col 7 (80%)** | **Col 8 (90%)** |
| | **$D_{out}$ on Mask/BFP [mm]** | **Light sheet thickness (FWHMxy) / length (FWHMz) [µm]** | | | | | | | |
| Row 1 | 6.0/1.920 | 0.60/4.9 | 0.525/5.0 | 0.50/5.5 | 0.45/6.0 | 0.43/7.0 | 0.40/8.6 | 0.39/12.0 | 0.37/18.0 |
| Row 2 | 4.0/1.280 | 0.80/10.0 | 0.76/11.0 | 0.70/12.0 | 0.65/13.5 | 0.62/15.0 | 0.59/18.1 | 0.565/25.7 | 0.54/43.7 |
| Row 3 | 3.2/1.024 | 0.97/15.0 | 0.925/16.4 | 0.875/17.5 | 0.83/20.0 | 0.78/24.0 | 0.74/30.3 | 0.70/41.2 | 0.67/68.0 |
| Row 4 | 2.8/0.896 | 1.10/18.0 | 1.03/20.0 | 0.99/23.0 | 0.94/25.0 | 0.88/30.0 | 0.83/40.4 | 0.81/53.7 | 0.765/90.0 |
| Row 5 | 2.4/0.768 | 1.27/25.7 | 1.16/29.0 | 1.15/31.4 | 1.10/35.4 | 1.05/42.9 | 0.99/53.0 | 0.945/70.0 | 0.91/118.0 |
| Row 6 | 2.0/0.640 | 1.46/37.0 | 1.39/40.0 | 1.34/43.3 | 1.29/50.6 | 1.20/57.2 | 1.14/72.0 | 1.10/102.0 | 0.99/188.0 |
| Row 7 | 1.6/0.512 | 1.84/57.0 | 1.72/62.7 | 1.57/66.0 | 1.54/76.0 | 1.45/87.0 | 1.35/110.0 | 1.28/157.0 | 1.10/254.0 |
| Row 8 | 1.2/0.384 | 2.23/96.0 | 2.16/106.0 | 2.11/120.0 | 2.02/132.0 | 1.73/150.0 | 1.62/185.0 | 1.64/252.0 | 1.42/380.0 |

**Table S1: Light sheet properties resulting from shaping the illumination beam with the GBM mask.** The light sheet properties are defined by the objective O1 and the magnification in the illumination beam path. The light sheet properties listed here were measured with using 488 nm light and the 100x/1.35 NA silicon oil objective (Olympus). The dimensions of the light sheets were measured in *xy* (thickness as FWHMxy) and *z* (length as FWHMz = 2 x Rayleigh Length). For each measurement, a given position of the GMB mask (row and column indexes, see Fig. S1) was moved in the beam path (Fig. 1B). In the GBM mask, $D_{in}$ is defined as a percentage of $D_{out}$ (see Fig. S1). In this table, the values for $D_{out}$ correspond to the physical size on the GBM mask, and to the physical size of the beam in the back focal plane of the objective (the ratio of these two sizes depends on the overall (de)magnification of the illumination system). In our optical system, the beam was first demagnified 4x (L1-L2 lenses) and then magnified 1.28x (SL-TL3 lenses). Hence, the overall beam magnifications was M = 1/3.125, i.e. the beam was demagnified 3.125x, and the true $D_{out}$ on the back focal plane was $D_{out}/3.125$. Note that the first demagnification was done after the beam passed through the GBM mask, because it is easier to align the incoming beam with a mask that has bigger holes than smaller ones.

| | Microscope | Slit Size / pinhole size | Beamshape and Dimension | Exposure | Excitation (Laserpower @ BFP) |
|---|---|---|---|---|---|
| **Figure 1** | | | | | |
| 1C | DC-APOM | 20 px | Bessel: FHWMxy = 1.15 µm; FHWMz = 31.4 µm | 0.48 ms | 488 nm (13.1 µW) |
| 1D, left | Widefield | not applicable | not applicable | 200 ms | Brightfield |
| 1D, right | DC-APOM | not applicable | not applicable | 100 ms | LED (see Appendix A) |
| **Figure 2** | | | | | |
| A, row 1, Biofilm | DC-APOM | 20 px | Gaussian: FHWMxy = 1.385 µm; FHWMz =30µm | 6.9 ms | 488 nm (100 µW) |
| A, row 1, PSF PVA | DC-APOM | none | Gaussian: FHWMxy = 1.385 µm; FHWMz =30µm | 2 s | 488 nm (1000 µW) |
| A, row 1, PSF Water | DC-APOM | none | Gaussian: FHWMxy = 1.385 µm; FHWMz =30µm | 2 s | 488 nm (1000 µW) |
| A, row 1, Biofilm | Spinning Disk Confocal | 50 µm | not applicable | 30 ms | 488 nm (400 µW) |
| A, row 1, PSF PVA | Spinning Disk Confocal | 50 µm | not applicable | 30 ms | 488 nm (600 µW) |
| A, row 1, PSF Water | Spinning Disk Confocal | 50 µm | not applicable | 30 ms | 488 nm (600 µW) |
| A, row 2, Biofilm | DC-APOM | 20 px | Gaussian: FHWMxy = 1.385 µm; FHWMz =30µm | 6.9 ms | 488 nm (50 µW) |
| A, row 2, PSF PVA | DC-APOM | none | Gaussian: FHWMxy = 1.385 µm; FHWMz =30µm | 1 s | 488 nm (1000 µW) |
| A, row 2, PSF water | DC-APOM | none | Gaussian: FHWMxy = 1.385 µm; FHWMz =30µm | 1 s | 488 nm (1000 µW) |
| A, row 2, Biofilm | Spinning Disk Confocal | 50 µm | not applicable | 30 ms | 488 nm (400 µW) |
| A, row 2, PSF PVA | Spinning Disk Confocal | 50 µm | not applicable | 30 ms | 488 nm (600 µW) |
| A, row 2, PSF water | Spinning Disk Confocal | 50 µm | not applicable | 30 ms | 488 nm (600 µW) |
| A, row 3, Biofilm | DC-APOM | 20 px | Gaussian: FHWMxy = 1.27 µm; FHWMz =25.7µm | 6.9 ms | 488 nm (12 µW) |
| A, row 3, PSF sil. oil | DC-APOM | none | Gaussian: FHWMxy = 1.235 µm; FHWMz =23µm | 2 s | 488 nm (15 µW) |
| A, row 3, PSF water | DC-APOM | none | Gaussian: FHWMxy = 1.235 µm; FHWMz =23µm | 2 s | 488 nm (15 µW) |
| A, row 3, Biofilm | Spinning Disk Confocal | 50 µm | not applicable | 30 ms | 488 nm (400 µW) |
| A, row 3, PSF sil. oil | Spinning Disk Confocal | 50 µm | not applicable | 30 ms | 488 nm (600 µW) |
| A, row 3, PSF water | Spinning Disk Confocal | 50 µm | not applicable | 30 ms | 488 nm (600 µW) |
| **Figure 3** | | | | | |
| Confocal | Spinning Disk Confocal | 50 µm | not applicable | 90 ms | 488 nm (281 µW) |
| Gaussian | DC-APOM | 20 px | Gaussian: FHWMxy = 1.27 µm; FHWMz =25.7µm | 0.48 ms | 488 nm (18 µW) |
| Bessel | DC-APOM | 20 px | Bessel: FHWMxy = 1.15 µm; FHWMz = 31.4 µm | 0.48 ms | 488 nm (13.1 µW) |
| **Figure 4** | | | | | |
| A: Dispersal | DC-APOM | 20 px | Bessel: FHWMxy = 1.15 µm; FHWMz = 31.4 µm | 6.9 ms | 488 nm (185 µW) |
| B: Osmotic Shock | DC-APOM | 20 px | Bessel: FHWMxy = 1.15 µm; FHWMz = 31.4 µm | 6.9 ms | 488 nm (100 µW) |
| C: Phagocytosis | DC-APOM | 20 px | Bessel: FHWMxy = 1.15 µm; FHWMz = 31.4 µm | 6.9 ms | 488nm (90 µW) 552nm (100µW) |
| **Figure S3** | | | | | |

| | | | | | |
|---|---|---|---|---|---|
| Gaussian | DC-APOM | none | Gaussian: FHWMxy = 2.231 µm; FHWMz =96µm | 400 ms | 488 nm (12 µW) |
| Gaussian | DC-APOM | 160 px | Gaussian: FHWMxy = 2.231 µm; FHWMz =96µm | 54.9 ms | 488 nm (12 µW) |
| Gaussian | DC-APOM | 40 px | Gaussian: FHWMxy = 2.231 µm; FHWMz =96µm | 13.7 ms | 488 nm (12 µW) |
| Gaussian | DC-APOM | 20 px | Gaussian: FHWMxy = 2.231 µm; FHWMz =96µm | 6.9 ms | 488 nm (12 µW) |
| Gaussian | DC-APOM | 10 px | Gaussian: FHWMxy = 2.231 µm; FHWMz =96µm | 3.4 ms | 488 nm (12 µW) |
| Bessel | DC-APOM | none | Bessel: FHWMxy = 1.292 µm; FHWMz = 50 µm | 400 ms | 488 nm (13 µW) |
| Bessel | DC-APOM | 80 px | Bessel: FHWMxy = 1.292 µm; FHWMz = 50 µm | 27.5 ms | 488 nm (13 µW) |
| Bessel | DC-APOM | 20 px | Bessel: FHWMxy = 1.292 µm; FHWMz = 50 µm | 6.9 ms | 488 nm (13 µW) |
| Bessel | DC-APOM | 10 px | Bessel: FHWMxy = 1.292 µm; FHWMz = 50 µm | 3.4 ms | 488 nm (13 µW) |
| Bessel | DC-APOM | 5 px | Bessel: FHWMxy = 1.292 µm; FHWMz = 50 µm | 1.7 ms | 488 nm (13 µW) |
| **Figure S4** | | | | | |
| Confocal | Spinning Disk Confocal | 50 µm | not applicable | 405 ms | 488 nm (55 µW) |
| Gaussian | DC-APOM | 20 px | Gaussian: FHWMxy = 1.27 µm; FHWMz =25.7µm | 0.48 ms | 488 nm (55 µW) |
| Bessel | DC-APOM | 20 px | Bessel: FHWMxy = 1.15 µm; FHWMz = 31.4 µm | 0.48 ms | 488 nm (55 µW) |

**Table S2: Microscope acquisition settings for the presented experimental datasets.** In case of DC-APOM the exposure times are given as the slit exposure time.

## References


1. A. Edelstein, N. Amodaj, K. Hoover, R. Vale, N. Stuurman, A. Edelstein, N. Amodaj, K. Hoover, R. Vale, and N. Stuurman, "Computer Control of Microscopes Using µManager," Curr. Protoc. Mol. Biol. 14.20.1-14.20.17 (2010).
2. A. D. Edelstein, M. A. Tsuchida, N. Amodaj, H. Pinkard, R. D. Vale, and N. Stuurman, "Advanced methods of microscope control using µManager software," J. Biol. Methods **1**, 10 (2014).
3. E. Baumgart and U. Kubitscheck, "Scanned light sheet microscopy with confocal slit detection," Opt. Express **20**, 21805 (2012).
4. B. Zhang, J. Zerubia, and J. C. Olivo-Marin, "Gaussian approximations of fluorescence microscope point-spread function models," in *Applied Optics* (OSA - The Optical Society, 2007), Vol. 46, pp. 1819–1829.
5. M. Gu, *Advanced Optical Imaging Theory* (Springer Science & Business Media, 2000), Vol. 75.
6. T. Li, S. Ota, J. Kim, Z. J. Wong, Y. Wang, X. Yin, and X. Zhang, "Axial plane optical microscopy.," Sci. Rep. **4**, 7253 (2014).
7. S. An, K. F. Ziegler, P. Zhang, Y. Wang, T. Kwok, F. Xu, C. Bi, S. Matosevic, P. Yin, T. Li, and F. Huang, "Axial plane single-molecule super-resolution microscopy of whole cells," Biomed. Opt. Express **11**, 461 (2020).